AGU100 ADVANCING EARTH AND SPACE SCIENCE

JGR Solid Earth

RESEARCH ARTICLE

10.1029/2018JB016878

Key Points:

- The friction constitutive law of Aharonov & Scholz (2018) is applied to high temperature and pressure: the experimental data are well fit
- The experimentally-constrained theory predicts transition from friction to low temperature plasticity at 300C for quartzo-felspathic rocks
- The transition from low to high temperature plastic flow will occur at 475C, forming a brittle ductile transition region several km thick

Correspondence to:
E. Aharonov,
einatah@mail.huji.ac.il

Citation:
Aharonov, E., & Scholz, C. H. (2019). The brittle-ductile transition predicted by a physics-based friction law. *Journal of Geophysical Research: Solid Earth*, *124*, 2721–2737. https://doi.org/10.1029/2018JB016878

Received 17 OCT 2018
Accepted 14 DEC 2018
Accepted article online 21 JAN 2019
Published online 9 MAR 2019

The Brittle-Ductile Transition Predicted by a Physics-Based Friction Law

Einat Aharonov[1] and **Christopher H. Scholz**[2]

[1]Institute of Earth Sciences, The Hebrew University, Jerusalem, Israel, [2]Lamont-Doherty Earth Observatory of Columbia University, Palisades, NY, USA

Abstract A theory of the brittle-ductile transition (BDT) is shown to be a direct consequence of a recently developed physics-based constitutive law for rock friction (Aharonov & Scholz, 2018, https://doi.org/10.1002/2016JB013829), which assumes exponential creep on contacts. The theory was previously tested against experimental data for sliding at low ambient temperature and stress. Here, theoretical interpretation of experimental data at high temperature and stress shows that at some point the real area of contact reaches a maximum value beyond which it becomes fixed. The constitutive law shows that this marks the onset of the BDT, beyond which sliding changes from frictional to an exponential flow law for low-temperature plasticity. Application to the Earth's crust shows that beyond this point, strength fall linearly with depth until it intersects the power law for bulk flow of the country rock, which marks the lower boundary of the BDT. Modeling, constrained by experimental data for granite, predicts that the BDT starts at a temperature of about 300°C, at a depth of 11–13 km in the continental crust, depending on fault slip rate and temperature gradient. The completion of the BDT is similarly calculated to occur around 475°, at 16–18 km, in agreement with laboratory and field observations. The BDT is thus found to be a region spanning about 175°C with a width of several kilometers. Within the exponential flow region, the structural outcome would be a relatively narrow mylonitized fault zone, which widens into a broader region of shear at the base of the BDT.

1. Introduction

1.1. The Nature of the Brittle-Ductile Transition

Geological observations indicate that the upper crust deforms by frictional faulting, whereas the lower crust deforms by crystal plastic flow. Thus, a simplified strength envelop for the crust was devised by combining a linear Coulomb friction law to describe the limiting stress of faulting with a power law creep law for the plastically deforming lower crust (Brace & Kohlstedt, 1980; Goetze & Evans, 1979). The point where these two curves meet is said to define the brittle-ductile transition (BDT). The BDT is also assumed to define the lower limit of seismic activity on active faults. The prediction of the BDT of this two-mechanism model corresponds reasonably well with the depth distribution of earthquakes on continental faults (Sibson, 1982) as well as the depth of the transition from cataclasite to mylonite associated with the onset of quartz plasticity in fault zones cutting quartzo-feldspathic rock (Stipp et al., 2002; Voll, 1976; S. White et al., 1980). A smoothed version was developed by Shimamoto and Noda (2014) and was used to explain halite data.

However, it is clear that this description is overly simplistic. For one thing, the power law creep law that is extrapolated from high-temperature lab measurements is not expected to be the flow regime at the low temperatures and high stresses near the BDT. In addition, both experimental (Hirth & Tullis, 1992, 1994) and field observations (Stipp et al., 2002) show that the BDT does not occur at a point but is a gradual transition involving an evolution of deformation mechanisms over a depth range corresponding to several hundred degrees Celsius. The experimental and field studies of quartz deformation find three regimes with increasing temperature: an onset of plasticity associated with dislocation glide and negligible climb and recovery, an intermediate mixed mode of deformation, and a high-temperature regime characterized by rapid dislocation climb and recovery. At geological strain rates, the first regime begins at ~300°C and the third regime at ~500°C (Stipp et al., 2002; Tullis, 2002). Although it is hazardous to identify micromechanisms with rheology, it is fair to say that power law creep, which fundamentally depends upon dislocation climb, can be associated with the highest temperature of these three regimes, which we infer correlates with the high-temperature creep regime. The lowest-temperature regime, at the onset of plasticity, must be associated with a flow law that allows thermally activated glide without rapid enough atomic diffusion to permit climb and

recovery. A rheology of this type, often called Peierls creep, which typically describes low temperature, high stress plasticity, is of the form (e.g., Chester, 1994; Evans & Goetze, 1979; Tsenn & Carter, 1987):

$$\dot{\varepsilon} = \varepsilon_0 \exp(-[Q-G]/RT) \quad (1)$$

Mei et al. (2010), in a strength model for the oceanic lithosphere, included a layer with a rheology of this type between the frictional and power law creep regimes. Here ε_0 is a constant, Q is activation energy, and G(τ) is some function of the stress τ.

These two- or three-mechanism models are not theories of the BDT, merely criteria that constrain its position. A theory of the BDT must include a mechanism that explicitly predicts it. Here we provide such a theory, based on a model of friction in which the deformation at the contact scale follows a flow law of the form of equation (1), as detailed in our first paper in this series, Aharonov and Scholz (2018), abbreviated hereafter as A&S18.

It is fundamental to such a model that the real area of contact, A_r, increases with contact time, normal stress, temperature, and with decreasing slip rate. Yet it is clear that the normalized real contact area (A_{rr}/A) cannot increase beyond 1 for sliding on discrete surfaces, since when the real area becomes equal to the nominal area, sliding transitions to bulk deformation and the sliding surfaces are no longer defined. We argue here that at some point, when A_r grows large enough, its value becomes restricted by other processes, so that it is no longer given by our starting contact model.

What are the processes that may restrict A_r? In most situations sliding actually occurs within a granular media, composed of the wear detritus known as fault gouge. In such cases competition between shear-induced dilation and creep-induced compaction (Chen & Spiers 2016; Marone et al., 1990; Niemeijer & Spiers, 2007) is expected to restrict A_r during steady state sliding, causing it to reach a limiting value of $A_r^{\mathrm{res}}/\mathrm{A} < 1$. Since the effect of normal stress is to inhibit dilatancy, the limiting value of real contact area, A_r^{res}/A, is expected to increase with normal stress. It will of course not exceed 1, even at the highest normal stress, and will not get to 0 at zero normal stress either. Another possible process for restricting A_r is competition between damage created during sliding, which reduces A_r, and creep-induced healing, which increases it (Siman-Tov et al., 2015). We do not know which of these processes controls the value of A_r^{res}, and thus, we do not know a priori the value of A_r^{res}, but we will presume such a value of A_r^{res}/A exists.

We claim, and show below, that once A_r saturates to its restricted value, A_r^{res}, the shear strength will no longer increase with normal stress but will remain constant, and the rheology changes from friction to a plastic flow law of the form (1). This point predicts the onset of the BDT zone—which we term the frictional-plastic transition (FPT). The lower limit of the BDT zone occurs where the exponential flow law intersects the power law creep law, which describes the bulk flow of the country rock.

1.2. The Goal of This Work

In A&S18 we derived a single, physics-based, friction law to explain and predict steady state friction in rocks. This model is general for all shear velocities (V), temperatures (T), normal stresses (σ_n), and materials. A&S18 test this model for quartz and granite across a wide range of slip velocities, under low normal stress and low ambient temperatures. We found that our model explains and predicts the major features of steady state rock friction over a range of slip rates from interseismic to coseismic.

In this paper we use the same model and the same material parameters that were used in A&S18 for the low T and low normal stress experiments but under high ambient temperatures and high normal stress. We compare the model predictions with the high-T and σ_n data for granite and quartzite of Hirth and Tullis (1994), Blanpied et al. (1995), and Chester and Higgs (1992), shown in Figure 1. The only free parameter that remains to fitting these data is $A_r^{\mathrm{res}}(\sigma_n)$. The value of A_r^{res} will be shown below to define both the FPT and the dependence of friction on ambient temperature in the plastic regime. Applying these results to the continental crust shows that the BDT zone is a region several kilometers thick with a lower bound given by the FPT and an upper bound at the transition from exponential creep to power law creep. Using the parameters determined by fitting the experimental data predicts a FPT at about 300°C, weakly dependent upon fault slip rate.

We argue that we may use quartz flow laws for granite, since at higher temperature the granite forms a mylonitic fabric where the quartz, which is plastically deforming, forms layers parallel to shear, separated by

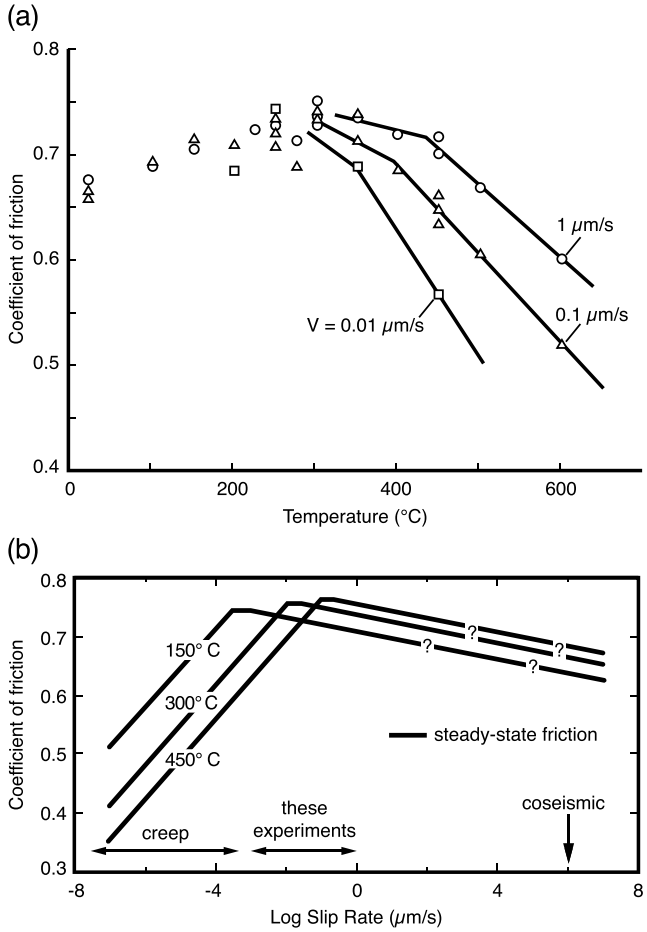

Figure 1. (a) Experimental friction of wet granite as function of ambient temperature T_0, for three different slip rates, from Blanpied et al. (1995). Below ~300 °C, friction increases with T_0 and is independent of slip rate. For T_0 greater than ~300 °C, friction decreases with increasing T_0 but increases strongly with increasing slip rate. (b) Figure 9 from Chester and Higgs (1992): Steady state friction versus log slip rate for different temperatures in wet ultrafine quartz gouge experiments. Behavior at low slip rates is dominated by plastic flow, whereas at high slip rates it is dominated by frictional slip. The transition between mechanisms is indicated by change in the slope of the lines. The transition occurs at higher slip rates for increasing temperatures. Behavior at very high slip rates was uncertain at that time.

feldspar (which behaves rigidly) layers, so the deformation is controlled by the weaker quartz layers. Such an assumption is supported by field observations (e.g., Behr & Platt 2011; Simpson, 1985).

2. Theory

The first two assumptions of theory are detailed in section 2 of A&S18 and briefly recapitulated here. The third assumption is a new one that is added here.

2.1. Assumption 1: Friction Arises From Creep of Contacts and Is Predictable From Contact Stresses

The model derived in A&S18 assumes that macroscopic friction arises from simultaneous shear and normal creep on a population of sliding contacts, following Bowden and Tabor (1950, 1964). It follows Heslot et al. (1994), Brechet and Estrin (1994), Baumberger and Caroli (2006), Rice et al. (2001), Nakatani (2001), and Putelat et al. (2011), in assuming that contact shear strength, τ_c, for sliding at a given slip rate V is controlled by a flow law of the form of equation (1), on the contact scale. Equation (2a) of A&S18 writes this assumption for contacts sliding at velocity V:

$$V = V_{\mathrm{smax}} \exp\left(-\frac{Q_s - \tau_c N\Omega_s}{RT_c}\right) \tag{2a}$$

where N is Avogadro number, T_c is the contact temperature, R the gas constant, and Q_s and Ω_s are the activation energy and activation volume for shear creep. V_{smax} is a reference velocity, the highest possible shear creep rate achieved when shear contact stresses, τ_c, is at its highest possible value $\tau_c = \tau_c^* = Q_s/N\Omega_s$. Equation (2a) is easily inverted to give the contact shear stress, τ_c, as function of V, T_c, and material parameters, providing equation (3b) below. Equations (2c) and (2d) of A&S18 derived the contact normal stress, σ_c, using a similar creep law but in the normal direction to the contact, that is, exponential normal creep causing contact convergence and contact area growth.

$$\frac{\mathrm{d}h}{\mathrm{d}t} = -V_{\mathrm{nmax}} \exp\left(-\frac{Q_v - \sigma_c N\Omega_v}{RT_c}\right); \tag{2b}$$

Here h is the asperity height and V_{nmax} is the reference (highest possible) contact-normal creep rates, achieved when contact normal stresses are at their highest possible value $Q_v/N\Omega_v$. Q_v and Ω_v are the activation energy and activation volume for normal creep.

From these assumptions, we obtained the shear (equation (3b)) and normal (equation (3a)) stresses on contacts in A&S18, there detailed in equations (3a)–(3e), and presented here again for completeness:

$$\sigma_c = \sigma_c^0\left(1 - b' \ln\left(1 + \frac{d}{Vt_c}\right)\right) \tag{3a}$$

$$\tau_c = \tau_c^*\left(1 + a' \ln\left(\frac{V}{V_{\mathrm{smax}}}\right)\right) \tag{3b}$$

$$\frac{A_r}{A} = \frac{\sigma_n}{\sigma_c^0}\frac{1}{\left(1 - b' \ln\left(1 + \frac{d}{Vt_c}\right)\right)} \tag{3c}$$

$$a' = \frac{RT_c}{Q_s};\ b' = \frac{RT_c}{BQ_v};\ \sigma_c^0 = \frac{Q_v B}{N\Omega_v};\ \tau_c^* = \frac{Q_s}{N\Omega_s};\ E_{tc} = Q_v - N\Omega_v\sigma_c^0 = (1-B)Q_v \tag{3d}$$

Table 1
Table of Parameters, Definitions, and Values

Parameter	Symbol	Value (run 4)	Units	Ref
volumetric activation volume	Ω_v	$5 * 10^{-29}$	m^3	Nakatani (2001) and Rice et al. (2001)
surface activation volume	Ω_s	$7.8 * 10^{-29}$	m^3	Nakatani (2001) and Rice et al. (2001)
Volumetric activation energy	Q_v	240	KJ/mol	Nakatani (2001) and Rice et al. (2001)
Surface activation energy	Q_s	270	KJ/mol	Nakatani (2001) and Rice et al. (2001)
Prefactor	B	0.89 *exp(−0.006 *(T_0-273))	—	A&S18
Contact diameter	d	10	μm	Beeler et al. (2008)
Maximum shear rate	V_{smax}	$0.5c_s$		Noda (2008) and Rice et al. (2001)
Shear wave velocity	c_s	3,750	m/s	www.quartz.com
Reference cutoff time, at room T	t_{cr}	2	s	Dieterich (1972, 1978)
Thermal equilibration distance.	D_{th}	$C\sigma_n{}^q$, here $C = 5$, $q = -1$.	m	Di Toro et al. (2004, 2011)
Melting temperature	T_m	1,670	K	Rice (2006)
Ambient temperature	T_0	270–870	K	imposed
Heat capacity	C	730 * (1.7–200/T_c)	J/kg/K	Fitting Figure 4 of Vosteen and Schellschmidt (2003)
Thermal diffusivity	α	10^{-4}/T–0.5 * 10^{-7}	m^2/s	Fitting Figure 4 of Hanley et al. (1978), assuming 1-OM reduction by porosity
Density	ρ	2,650	Kg/m^3	
Contact temperature	T_c	300–1370	K	from equation (5)
Shear rate	V	10^{-12}–10	m/s	Imposed
Saturated contact area	A_r^{res}	0.07–0.98	—	from equation (9)
Applied normal stress	σ_n	5–2,500	MPa	
Steady state friction coefficient	μ	0.01–1	—	from equation (4)
Shear stress on contacts	τ_c		MPa	from equations (3a)–(3e)
Normal stress on contacts	σ_c		MPa	from equations (3a)–(3e)
viscous shear coefficient	a		—	from equations (3a)–(3e)
Contact-growth coefficient	b		—	from equations (3a)–(3e)
Avogadro number	N	$6 * 10^{23}$	1/mol	
Gas constant	R	8.3	J/mol/K	
Shear modulus	G	$31{\cdot}10^9$	Pa	

$$t_c = b' \frac{d}{V_{nmax}} \exp\left(\frac{E_{tc}}{RT_c}\right) \tag{3e}$$

The real contact area, A_r, normalized by nominal area A, in equation (3c), was derived from the relation $A_r\sigma_c = A\sigma_n$. The constants given in (3d) and (3e) were derived and their significance explained in A&S18. All parameters and corresponding symbols are given in Table 1 of A&S18. For completeness they are briefly presented here again in Table 1: t_c is the "cutoff time" (Nakatani & Scholz, 2004a, 2004b), which is thermally activated with activation energy, E_{tc}. The σ_c^0 is the contact stress at time $t = 0$, meaning the ab initio contact stress. In A&S18 it is called the "indentation hardness" at time $t = 0$. B is a prefactor between 0 and 1, whose value decreases with temperature to account for the decrease of σ_c^0 with temperature, following experimental observations (Evans, 1984). Activation energy, Q_s, and activation volume, Ω_s, for surface creep, may differ from the normal direction (or asperity flattening) creep parameters, Q_v and Ω_v, since those describe volumetric creep (as explained in A&S18). The d is contact diameter.

One may obtain the friction coefficient, $\mu = \frac{\tau_c}{\sigma_c}$, by dividing equation (3b) by equation (3a). Using $A_r\sigma_c = A\sigma_n$, one may alternatively express the friction coefficient via the contact area instead of via σ_c.

$$\mu = \frac{A_r}{A}\frac{\tau_c}{\sigma_n} \tag{4}$$

This form better serves our purposes here, and equation (4) will be used in this paper to obtain friction. Note that it is the full solution for friction, that holds for all temperatures, normal stresses and velocities.

2.2. Assumption 2: Steady State Temperature and Friction

We assume sliding is steady when both friction and contact temperature reach steady state. The steady state temperature of the contacts (A&S18, equation 5) is rewritten here for completeness:

$$T_c = T_0 + \frac{\tau_c}{\rho C}\sqrt{\frac{V}{\pi\alpha}}\left[\sqrt{d} + \frac{\sigma_n}{\sigma_c}\sqrt{D_{\text{th}}}\right] \tag{5}$$

where T_0 is the ambient temperature, D_{th} the thermal distance over which the sliding surface achieves thermal steady state (Di Toro et al., 2011), C is the heat capacity, α the thermal diffusivity, and ρ the density.

When slip rate is fast enough (seismic), equation (5) predicts that the contacts reach melting temperature, T_m. Thermodynamic considerations dictate that T cannot exceed T_m, even if V is increased further. In this case we assume that steady state sliding occurs at $T_c = T_m$ and that shear stress is reduced to compensate and maintain steady state, following equation (6) in A&S18.

2.3. Assumption 3: Plasticity Onset When Contact Area Saturates

When the ambient temperature and the applied normal stress are high, contact behavior changes and so does friction. In nature it is observed that above a certain ambient temperature and normal stress, the fault zone becomes a mylonite zone; that is, the fault transits to fully plastic flow. To capture plastic flow physics in our model, we add now a single physical assumption, guided by experimental data, that at some point, at high enough σ_n, T_c,and long enough hold times, or low enough sliding rate, the real area of contact, A_r, in equation (3c), must reach a maximum value, A_r^{res}, such that it cannot increase further. Here we assume that A_r^{res} increases with σ_n. This agrees with the assumption that A_r^{res} is set by a competition between compaction and dilation but that dilation is restricted by normal stress. We assume A_r^{res} is independent of temperature, which fits the experimental data.

We next predict theoretically that the single assumption of the existence of an A_r^{res} leads in our model to two fundamental findings: (i) The point of contact area saturation coincides with the FPT since it leads to a weak dependence of strength on normal stress and (ii) the rheology then changes from frictional sliding, to low-temperature plastic flow law of the form of equation (1). To demonstrate, we calculate the friction of rocks at the two sides of the FPT from equation (4). Equation (4) gives the general form for friction, both during frictional and low-temperature plastic deformation, since its derivation did not decide yet what is A_r. The following shows that both frictional and plastic behaviors arise from equation (4)—frictional behavior occurs when A_r evolves and plastic when A_r saturates to $A_r^{\text{res.}}$

Frictional regime: In this regime A_r evolves with V and T_c according to equation (3c). Plugging equation (3c) into the friction equation (4) gives the steady state friction coefficient in the frictional sliding regime, μ^f:

$$\mu^f = \frac{\tau_c^*\left(1 + a' \ln\left(\frac{V}{V_{\text{smax}}}\right)\right)}{\sigma_c^0\left(1 - b' \ln\left(1 + \frac{d}{Vt_c}\right)\right)} \tag{6a}$$

Taylor expanding equation (6a), assuming the $b'\ln\left(1 + \frac{d}{Vt_c}\right)$ term is small, yields

$$\mu^f \sim \mu_0 + a^* \ln\left(\frac{V}{V_{\text{smax}}}\right) + b^* \ln\left(1 + \frac{d}{t_c V}\right) \tag{6b}$$

$$a^* = a'\mu_0 = \mu_0 \frac{RT_c}{Q_s};\ \ b^* = b'\mu_0 = \mu_0 \frac{RT_c}{BQ_v};\ \ \mu_0 = \frac{\tau_c^*}{\sigma_c^0} = \frac{Q_s}{BQ_V}\frac{\Omega_V}{\Omega_S} \tag{6c}$$

Equation (6b) gives the first-order approximation of equation (4b) of A&S18. We call the friction coefficient here μ^f, although in A&S18 it is called simply μ, to distinguish it here from the "plastic friction coefficient" μ^p, that will be discussed in the next subsection.

The a^* term, defined as the *viscous shear term* in A&S18, comes from the contact shear stress dependence on V (equation (3b)). The b^* term, termed the *contact area growth term* in A&S18, comes from the A_r dependence on V (equation (3c)).

The shear strength in the frictional regime, τ_{ss}^{f}, is simply the friction coefficient in equation (6b), μ_{ss}^{f}, multiplied by the applied normal stress σ_n:

$$\tau^f \sim \sigma_n \left(\mu_0 + a^* \ln\left(\frac{V}{V_{smax}}\right) + b^* \ln\left(1 + \frac{d}{t_c V}\right)\right) \tag{6d}$$

Thus, the shear strength in the frictional regime increases linearly with applied normal stress and has both a and b terms. In this regime friction can be either velocity weakening or strengthening, and will follow rate and state friction law, as derived in A&S18.

Low-temperature plastic regime: here instead of the growth equation for A_r (equation (3c)), used in the frictional regime, we use $A_r = A_r^{res}$ in equation (4). Again equation (3b) is used for τ_c. In this regime the plastic friction coefficient μ^p and the plastic shear strength τ^p are as follows:

$$\mu^p = \mu_0 + a^* \ln\left(\frac{V}{V_{smax}}\right) \tag{7a}$$

$$\mu_0 = \frac{A_r^{res}}{A\sigma_n}\frac{Q_s}{N\Omega_s}; \qquad a^* = \frac{A_r^{res}}{A\sigma_n}\frac{RT_c}{N\Omega_s} \tag{7b}$$

$$\tau^p = \sigma_n\left(\mu_0 + a^* \ln\left(\frac{V}{V_{smax}}\right)\right) = \frac{A_r^{res}}{AN\Omega_s}\left(Q_s + RT_c \ln\left(\frac{V}{V_{smax}}\right)\right) \tag{7c}$$

Equations (7a)–(7c) show that in the plastic regime steady state friction and strength are only controlled by the viscous term (the a^* term), while the b^* term (the contact area growth term) dropped out. The a^* term is always negative (V always smaller than V_{smax}), and its magnitude decreases with increasing slip rate. Thus, friction and strength are always V strengthening, and there is no velocity weakening in plastic slip, except that produced by thermal softening at high slip rate (as explained in the Discussion of A&S18).

Equation (7c) shows that the shear strength, τ^p, in this regime depends on normal stress only via the $\frac{A_r^{res}}{A}$ term. If $\frac{A_r^{res}}{A}$ grows slowly with σ_n then shear strength is nearly independent of σ_n, which indeed is a property characteristic of plastic deformation.

Finally, we demonstrate that a plastic flow law of the form equation (1) describes the plastic flow regime, by inverting equation (7c) to obtain sliding rate as function of the macroscopic shear stress τ^p :

$$V = V_{smax} \exp\left(-\frac{Q_s - \frac{A}{A_r^{res}} N\Omega_s \tau^p}{RT_c}\right) \tag{8}$$

Thus, our model is expected to capture the low-T plastic behavior of rocks below the FPT.

3. Method and Parameter Values

This paper explores our model for steady sliding under elevated ambient temperature, T_0, ranging between 0 and 600°C and applied normal stress, σ_n, ranging between 5 and 2,500 MPa, to probe conditions relevant for different depths in the Earth's crust, as well as compare to available experimental data. Similar to A&S18, we numerically solve coupled equations (3a)–(3e) to (5) (and equation 6 from A&S18 in case melting is reached), seeking a coupled dynamic steady state solution for contact stresses and contact temperature, by iterative solutions using a Matlab subroutine that we wrote. Details of solution technique and treatment of melting contacts are given in A&S18.

The difference from A&S18 is that here we add the assumption of a saturation value for A_r, A_r^{res}. This assumption is added since, as opposed to A&S18 that tested only low stresses and ambient temperatures, this paper tests friction and strength under high normal stresses and high ambient temperatures. These conditions are expected to considerably increase the value of real contact area relative to values in A&S18.

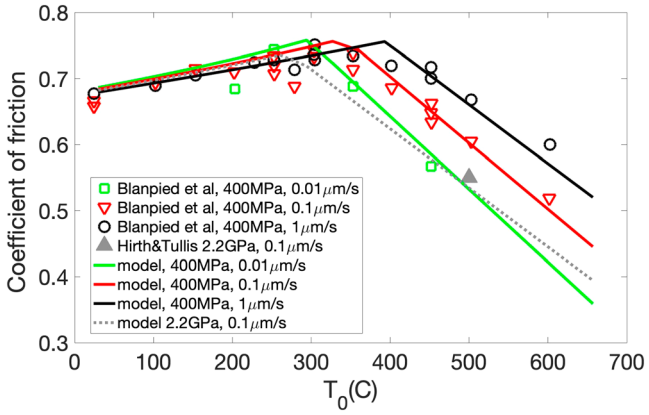

Figure 2. Experimental friction of wet granite as function of ambient temperature, T_0, for three different slip rates, from Blanpied et al. (1995), in symbols (same data as in Figure 1a). Also plotted is friction measured by Hirth and Tullis (1994) during steady deformation of wet quartz aggregates at 2.25-GPa normal stress, 500 °C and sliding rate of 0.1 μm/s. Note that the y axis, though labeled friction, is shear stress divided by a constant normal stress of 400 MPa for Blanpied et al. data and divided by 2.2 GPa for the Hirth and Tullis data. In the frictional regime, it is appropriate to refer to this as the friction coefficient, but in the plastic regime it should be referred to as the shear strength. Model results are plotted in lines. The temperature of the friction-plastic transition (FPT), T_{FPT}, appears here as a peak in friction, whose position is a function of slip rate and normal stress. For $T_0 < T_{\mathrm{FPT}}$ friction increases with T_0 but is nearly independent of slip rate (only second-order rate and state effects). For $T_0 > T_{\mathrm{FPT}}$ the strength decreases strongly with ambient temperature yet increases with slip rate.

We use thermodynamically and mechanically constrained values of parameters, as detailed in A&S18, for quartz and granite. Simulations were ran using the parameters of run 4 from A&S18, as detailed in Table 1 below. Although at low T_0 the behavior of all the runs in A&S18 differed only slightly (see Figures 5 and 7 in A&S18) the differences between runs are accentuated at higher T_0, and run 4 provided the best fit to the high T and stress experiments.

4. Results

4.1. Steady State Friction at Elevated Temperatures and Normal Stresses

We first model steady sliding friction at three different slip rates, as function of T_0 (between 0 and 650°C), under $\sigma_n = 400$ MPa, to compare with the Blanpied et al. (1995) experimental data of granite friction presented in Figure 1a. In fitting the data, we use the parameters of run 4 (see Table 1). The only free parameter in our model is A_r^{res},determined by data fitting. Figure 2 presents the experimental data (symbols) together with our model results using $\frac{A_r^{\mathrm{res}}}{A} = 0.096$. Note that in this figure the ordinate is labeled friction, but it really represents shear stress divided by a constant value of normal stress of 400 MPa. Below the FPT it can properly be interpreted as the friction coefficient; above it describes the plastic shear strength, the value of which is that number times 400 MPa.

Figure 2 shows that the model fits the entire data set. It predicts that friction increases with T_0 up to a peak value that corresponds to the FPT. Within that region friction has only a minor dependence on velocity, as expected from rate and state friction. Above that point, which we define as T_{FPT}, the theory accurately predicts the strong weakening with temperature and the strong velocity strengthening observed in the data. Changing the sole free parameter, $\frac{A_r^{\mathrm{res}}}{A}$, has two effects on the model curves in Figure 2: First, it shifts T_{FPT} left or right, and second it changes the slope of friction (or strength) versus ambient temperatures both below and above the FPT.

The excellent agreement between the Blanpied et al. (1995) experiments and our simulations lends confidence to our model and the value of $\frac{A_r^{\mathrm{res}}}{A}$at σ_n=400 MPa, given the fact that the model fits three nonmonotonic curves with only one (semi) free (semifree since $0<\frac{A_r^{\mathrm{res}}}{A}<1$), and since once it is chosen to fit one slip rate, $\frac{A_r^{\mathrm{res}}}{A}$ cannot be tuned further to adjust the locations of T_{FPT}, and to fit the other curves for the other slip rates.

We test our theory also at much higher σ_{n} using experimental results reported by Hirth and Tullis (1994). Their Figure 4 supplies one steady state data point for strength, measured at 500 °C and $\sigma_3 = 1$ GPa, at 0.1 μm/s. Using their reported fault angle (45°), we calculate $\tau = 1.25$ GPa and σ_n=2.25 GPa, which gives $\mu = 0.55$ (i.e., shear strength remains high at elevated pressure). This data point is added to Figure 2. We fit our model to this data point, using equations (3b) and (4), assuming plasticity prevails at this pressure and temperature, and so the contact area saturates. Again our only free parameter in fitting the data is $\frac{A_r^{\mathrm{res}}}{A}$, with best fit of $\frac{A_r^{\mathrm{res}}}{A} = 0.5$. The dashed line presents the model prediction under pressure of 2.25 GPa and sliding rate of 0.1 μm/s, using $\frac{A_r^{\mathrm{res}}}{A} = 0.5$, predicting that the transition to plasticity at these conditions occurs at ~250 °C.

The two different experimental results suggest that $\frac{A_r^{\mathrm{res}}}{A}$ increases with σ_n, which makes sense according, for example, to the idea where $\frac{A_r^{\mathrm{res}}}{A}$ is determined by a competition between dilation and compaction. We assume that $\frac{A_r^{\mathrm{res}}}{A}$ is independent of T_0, since the best fit to all the data we have is obtained under this assumption.

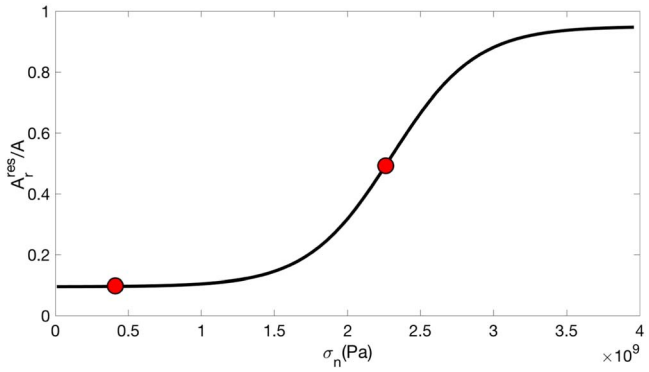

Figure 3. Value of saturated (normalized) real contact area A_r^{res}/A as function of nominal normal stress, as assumed in the model. The two red dots indicate the A_r^{res}/A values obtained from best fits to Figure 2: The value of A_r^{res}/A =0.096 provides the best fit of our model to the Blanpied et al. (1995), set of experiments at 400 MPa, while A_r^{res}/A =0.5 provides the best fit to the Hirth and Tullis (1994) experiments at 2.2 GPa. The A_r^{res}/A function (equation (9)) was chosen so that it passes through these two points and also asymptotes to 1 at high stress and to a lower value at zero stress.

To model strength for the range of stresses and temperature in the crust (as we do below), we require a functional dependence of $\frac{A_r^{res}}{A}$ on pressure. We shall assume a tan*h* function:

$$\frac{A_r^{res}}{A} = 0.95\left(0.55 + 0.45\ \tanh\left(\frac{\sigma_n - 2.3*10^9}{2.3*10^9}\right)\right) \quad (9)$$

This function, plotted in Figure 3, was chosen so that it satisfies the Blanpied et al. and the Hirth and Tullis constraints (two red dots in Figure 3) and also asymptotes to 1 at high stress and to a lower value at zero stress. This function is not unique: It is based on only two data points. More experiments of friction as a function of T_0 and σ_n are needed to further define it.

Because the BDT in the continental crust initiates at around 15 km, at a normal stress of about 450 MPa, we focus much of our discussion on conditions below and around this stress. Under these conditions, the value of $\frac{A_r^{res}}{A}$ is approximately constant (at 0.096) and we can ignore the increase of $\frac{A_r^{res}}{A}$ at higher normal stresses indicated in the data of Hirth and Tullis (1994).

Figure 4 shows the inner workings of our model with a plot of A_r/A versus T_0 for the 400-MPa experiments presented in Figure 2. The real area of contact, A_r/A, increases with T_0. A_r reaches the value of A_r^{res} at T_{FPT}, and for all $T > T_{FPT}$ the real contact area saturates and remains at the value A_r^{res}. T_{FPT} increases with V because at higher velocity there is less time for A_r to grow at a given T_0.

We next explore the FPT and behaviors on both sides of it by obtaining the shear strength, τ, as function of applied normal stress σ_n for various slip rates and various ambient temperatures T_0. Model results are presented in Figure 5. The FPT appears as a transition from a linear relation between τ and σ_n (i.e., frictional behavior) prevailing at low σ_n, (equation (6d)) to sliding at a nearly constant τ, independent of σ_n, at high σ_n (equation (7c)). The normal stress at which the FPT occurs increases with decreasing T_0, and with increasing slip rate V, as expected from experiments. For example, at T_0 = 250 °C plasticity appears at ~420 MPa when sliding at V = 0.001 μm/s, but no plasticity is seen when sliding faster at room temperature. At T_0 = 500 °C plasticity appears at ~210 Mpa for V = 0.001 μm/s and at ~320 Mpa for V = 0.1 μm/s. The physics for the normal stress dependence of the FPT is the same as that controlling the temperature dependence of the FPT seen in Figures 2 and 4.

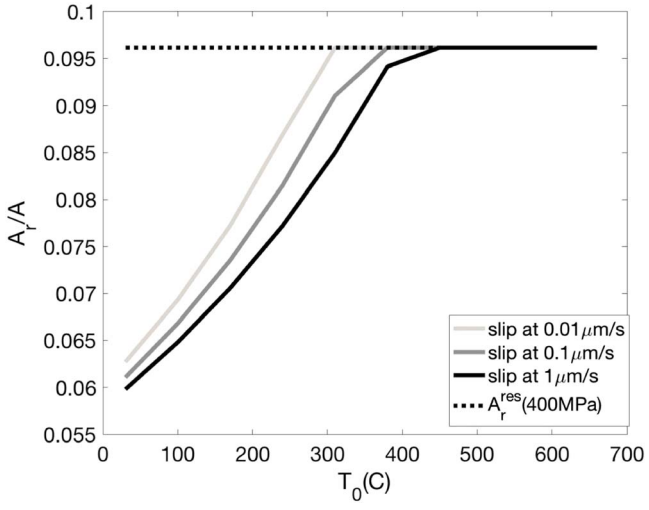

Figure 4. The working of our model for the data in Figure 2: Solid lines plot normalized contact area versus T_0, for the three slip rates of Blanpied et al. (1995), at 400 MPa. The dashed line shows the constant value of A_r^{res} = 0.096 at 400 MPa. Contact area increases sharply with increasing T_0, until it saturates to A_r^{res}, at which point the system undergoes a FPT. T_{FPT} increases with slip rate, since slower sliding contacts have more time for contact area growth, resulting in a larger contact area for a given T_0.

Note that although strength appears constant in Figure 5 in the regime above the FPT, it actually starts to climb again at about 1.5 GPa, following the dependence of $\frac{A_r^{res}}{A}$ on stress in the plastic regime (Figure 3), which enters into equation (7c). This high stress part of the curve is not shown, since we concentrate on the range relevant for low-temperature plasticity in the upper crust.

We also modeled friction under the Blanpied et al. (1995) experimental conditions for slip at other rates, in addition to the three slip rates shown in Figure 2. Figure 6a plots friction as function of slip rate at 400 Mpa, with different curves representing sliding at different ambient temperatures, ranging from room temperature to 520 °C. Model results show that at T_0 < 240 °C sliding is still fully frictional, following the frictional behavior explored in A&S18. Plasticity starts to appear at T_0 = 240 °C, but only at very slow slip rates, $V < 3*10^{-10}$ m/s. A plastic to friction transition (PFT) occurs at $V = 3*10^{-10}$ m/s and is observed here via a change in slope of friction as function of velocity: While the frictional slip at

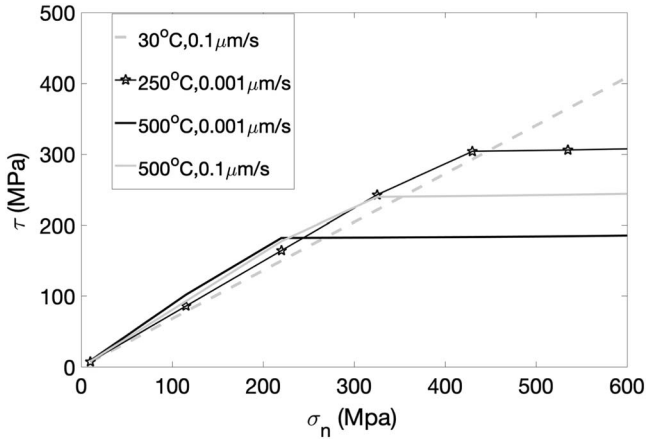

Figure 5. Model results for shear strength at a given slip rate and ambient temperature versus the applied normal stress. The friction-plastic transition appears as a transition from linear dependence between shear stress and normal stress (equation (6d)) to a nearly constant shear stress (equation (7c)). (Note that strength will start to climb again at about 1.5 GPa, following the dependence of $\frac{A_r^{res}}{A}$ on stress (Figure 3), but here only the low stress part of the curve is shown since this is the range relevant for the low T plasticity in the upper crust.) The normal stress at which the friction-plastic transition occurs increases with decreasing T_0 and increasing slip rate, similar to the process explained in Figures 3 and 4.

$V > 3*10^{-10}$ m/s is V weakening, for $V < 3*10^{-10}$ m/s plastic slip produces strong velocity strengthening (as predicted in equations (7a)–(7c)). We term the velocity at which the plastic to frictional transition occurs at a given T_0, $V_{FPT}(T_0)$. V_{FPT} increases rapidly with ambient temperature: V_{FPT} (240 °C) ~ $3 * 10^{-10}$ m/s, V_{FPT} (310 °C) ~ $3 * 10^{-8}$ m/s. At T_0 exceeding 450 °C sliding is fully plastic at all slip rates we tried. Even though sliding is fully plastic at all V for this T_0, we see that not all slip rates are V strengthening. The V weakening observed at high V in the plastic regime arises from thermal softening due to shear heating effects, as explained in section 6 of A&S18. Our predictions agree with the experimental results of Chester and Higgs (1992; presented here in Figure 1b), showing similar abrupt inversion of slope at the FPT, and similar increase in V_{FPT} with increasing T_0 (i.e., the inversion point moves to the right as T_0 increases).

Figure 6b shows the relative contact area, A_r/A, as function of slip rate for some of the runs in Figure 6a. The circles depict the constant value of saturated contact area, $A^{res}/A = 0.096$, at 400 MPa. Figure 6b shows that at room temperature, contact area varies with slip rate, since slip is fully frictional (A_r is smaller than A_r^{res} for all slip rates). For $T_0 = 240$ °C, at low enough slip rates, the elevated T_0 and the long contact duration during slow sliding, allow A_r to reach its saturation value A_r^{res}. This is the reason for the plastic regime at the very low slip rates at this temperature. Increasing T_0 even further enhances contact growth (equations (3a)–(3e)), so plastic slip dominates sliding at increasingly larger slip rates, until at $T_0 > 500$ °C sliding occurs always at saturated contact area, independent of slip rate (overlapping curves for A_r at 520 °C and A_r^{res}).

4.2. Steady State Friction as Function of Depth in the Crust

We used our model to simulate friction at normal stress and temperature values representing different depths in the crust. T_0 and σ_n were calculated using a geothermal gradient of 25 °C/km and effective normal stress gradient of 29.75 MPa/km. This value is obtained by assuming rock density of 2,700 kg/m^3, and subtracting hydrostatic pressure, giving 17 MPa/Km for the effective vertical stress. For thrust faults the effective normal stress on the fault plane is 1.75 times the effective vertical stress (e.g., equation 8.35 in Turcotte & Schubert, 2014). This gives the value of 29.75 MPa/km for an effective normal stress gradient which is appropriate for thrust or strike-slip faulting coincident with thrusting. Figure 7 plots friction as function of slip rate, where the different curves are calculations at depths of 6, 9, 11, 13, and 15 km. The dependence of friction on slip rate varies with depth. Descending from the surface to 9 km the absolute value of the friction coefficient increases, but it also becomes increasingly V weakening with depth (i.e., friction is more V weakening at 9 km than at 6 km). This increasing velocity weakening with depth arises when volumetric and surface activation energies are different (see equation 8 in A&S18), leading to a growth in (a-b) as temperature increases with depth.

Plasticity starts at about 11 km, but it has a unique form: While at very low slip rates, for $V < 10^{-10}$ m/s, slip is plastic and V strengthening, slip remains frictional at higher slip rates. This is the same behavior as seen and explained in Figure 6 and Figure 1b.

Descending deeper into the crust, plasticity dominates higher and higher slip rates, until at a depth of ~15 km, slip becomes fully plastic (exponential plasticity) at all rates that are relevant for earthquake nucleation. However, even for this fully plastic slip, strength does not monotonically increase with V as expected from plastic flow at constant temperature: At high enough sliding rate, when V exceeds the thermal velocity V_t (here ~10 μm/s), friction undergoes thermal softening. The thermal velocity V_t is defined and discussed in A&S18.

5. The BDT Zone in the Earth

5.1. The BDT Calculated From Theory

We may use our model to gain new insight regarding the BDT in the continental crust. Figure 8 plots shear strength for faults with three different geological slip rates as function of depth. It plots our calculations from

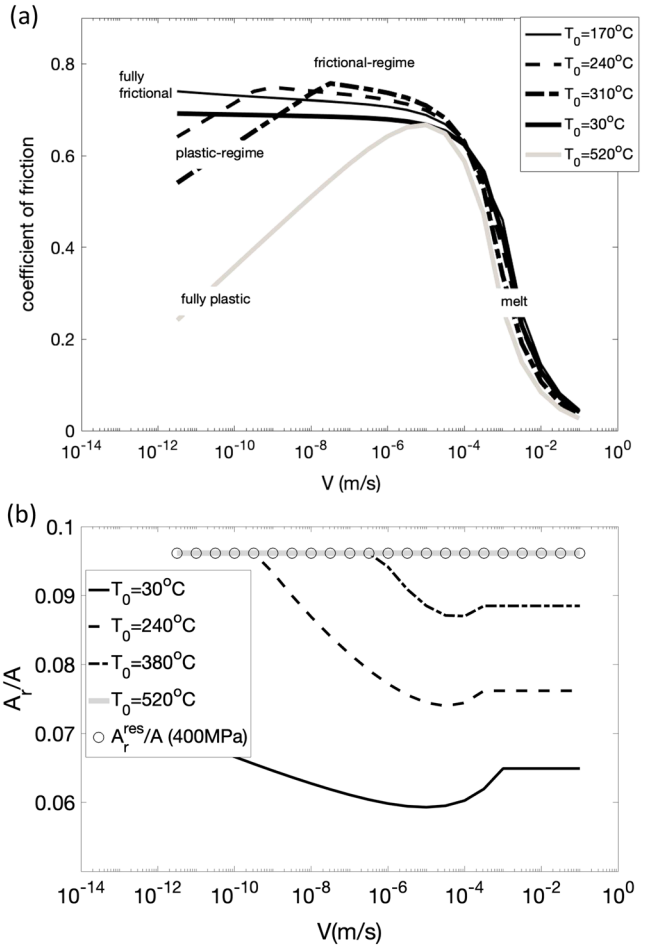

Figure 6. (a) Model results for steady state friction as function of slip rate, for various ambient temperatures, at σ_n = 400 MPa. Below 240 °C sliding is fully frictional at the slip rates tested here. At 240 °C slip becomes plastic for V slower than ~0.0003 μm/s. As T_0 increases, plasticity extends to higher and higher slip rates, as seen in the Chester et al. experiments in Figure 1b, until at about 500 °C sliding becomes fully plastic at all slip rates. At this high temperature, although sliding is fully plastic, still thermal-weakening sets in at high enough V. (b) Normalized real contact area, A_r/A for some of the runs in (a). The circles depict the restricted value of real contact area at 400 MPa, from equation (9), $A_r^{res} = 0.096$. At room temperature sliding is fully frictional, presenting a variable (unsaturated) contact area with slip rate. Slip becomes plastic, that is, A_r reaches its saturated value A_r^{res}, at 240 °C but only for very slow slip, for V < 0.0003 μm/s. As T_0 increases, slip at saturated contact area, and thus plasticity control higher and higher slip rates, until at about 500 °C sliding is fully plastic at all slip rates, seen here as sliding at $A_r = A_r^{res}$ at all slip rates.

our friction law, which exhibits the FPT and the exponential flow law beyond it (solid lines). We then extrapolate the experimental flow law for power law creep of wet quartzite (Hirth et al., 2001) to determine the lower boundary of the BDT.

As explained for Figure 7, T_0 and σ_n for each depth were calculated using geothermal gradient of 25 °C/km and normal stress gradient of 29.75 MPa/km. We use slip rate for faults in the frictional and plastic regimes, as obtained from our model. For the power law regime beneath, we use strain rates by assuming reasonable widths of shear zones at that depth. The three slip rates we used are 0.3, 3, and 30 mm/year. They represent geologic slip rates for active faults, corresponding to slow intraplate, fast intraplate, and interplate faults, respectively. These velocities are converted to strain rates in the plastic shear zones, assuming their thickness is in the range of several hundred meters to a kilometer (e.g., Beeler et al., 2016; Stipp et al., 2002). The width of the shear zones is assumed to increase with slip rate because that usually correlates with total slip and there are indications that the width of shear zones generally increases with net slip (e.g., Hull, 1988).

Our model predicts three regimes: down to about 10- to 12-km strength of the shallow crust follows a nearly linear friction law, as in Byerlee, equation (6d). The linear increase of τ with depth is dictated by the linearly increasing σ_n. μ_0 dominates equation (6d) and the a and b terms are small in comparison, so their increase with temperature contributes only a very slight concavity to the lower part of the curves. Because we find that $Ar/A \sim 0.1$ at the BDT, the effective stress law parameter $\alpha \sim 0.9$, so that large deviation from the simple effective stress law, as discussed by Hirth and Beeler (2015), will not occur.

Strength peaks at around 10–12 km (depending on slip rate and on the geotherm assumed) where transition to plasticity occurs due to saturated contact area. This ductility is low-temperature plasticity, occurring via exponential creep of contacts. It has a different dependence on depth than power law flow. The exponential creep produces a linear strength drop with depth, as explained and derived mathematically in section 6.6. Exponential creep then extends down until it intersects the power law creep flow law, depicted as dashed lines, calculated from the quartzite power law creep law derived from experiments (Hirth et al., 2001). The dashed lines are inversion of the power law to obtain stress from strain rate following:

$$\tau = \left(\frac{\dot{\varepsilon}}{k f_{H_2O}^m}\right)^{\frac{1}{n}} \exp\left(\frac{Q}{nRT}\right) \quad (10)$$

where $\dot{\varepsilon}$ is strain rate, taken as 10^{-13}, $3 * 10^{-13}$, 10^{-12} 1/s, from assuming 0.3, 3, and 30 mm/year slip distributed over a shear zone that is 100, 300, and 1,000 m wide, respectively. The other variables are taken from Hirth et al. (2001): $f_{H_2O}^m$ is water fugacity to power m, where $m = 1$ and $f_{H_2O} = 37$ MPa. The stress exponent $n = 4$, and prefactor $k = 10^{-11.2}$ MPa^{-n}/s. The activation energy is taken as $Q = 135$ KJ/mol. One can see that these lines intersect the exponential creep law before they intersect the friction curve. The exact location of this transition between exponential creep and power law creep depends on the geotherm, stress gradient, slip rate, shear zone width, and other model parameters (not shown). Below the exponential to power law transition, power law creep dominates the deformation since it predicts lower strength for the same slip rate.

Note that the intermediate flow regime 2 of Hirth and Tullis (1992) is expected to initiate at about 400 °C (Stipp et al., 2002; Tullis, 2002) and therefore should be included in the BDT region. This regime

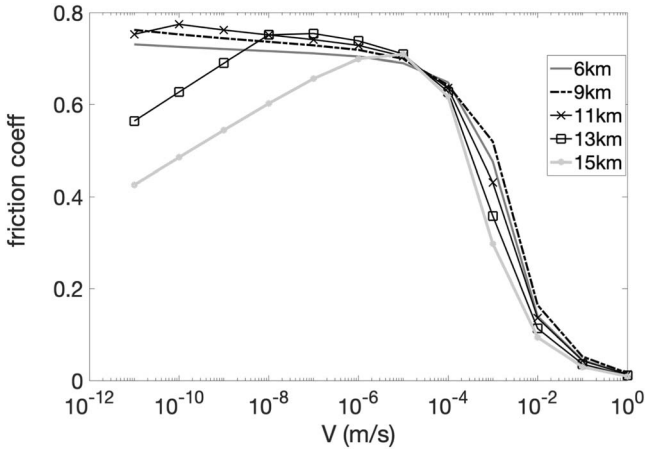

Figure 7. Modeled friction in quartz/granite, as function of slip rate, for different depths in the crust. Ambient temperature and normal stress for each curve are calculated from geothermal and effective normal stress gradients of 25 °C/km and 29.75 MPa/km, respectively. Descending from the surface to 9-km depth, the friction coefficient increases slightly but also becomes increasingly velocity weakening with depth. Below 11 km, granite creeps plastically at very slow (geological) slip rates but still slides frictionally and thermally weakens when sliding faster. This is seen as a change in slope at the plastic-friction transition (FPT) slip rate, V_{FPT}. $V_{FPT} = 0.0001$ μm/s at 11 km. Going deeper, ductility dominates higher and higher slip rates, so $V_{FPT} = 0.01$ μm/s at 13-km depth. Sliding at 15 km is fully plastic at all slip rates that are relevant for earthquake nucleation. The term plasticity refers here to low-temperature exponential plasticity.

presumably has some intermediate flow law, which is unknown. Including it would result in the strength curve becoming nonlinear above 400°, but this is expected to have little effect on the intersection with the high-temperature power law creep lines.

Thus, we have three zones, a shallow frictional zone which at a well-defined depth gives way to the FPT zone, characterized by the low-temperature exponential flow law which in turn gives way, at greater depth, to a power law creep regime characteristic of high-temperature plastic flow. The BDT thus does not occur at a point but over a width characterized by a span of temperatures. This is just as expected by experimental studies on quartz plasticity (Hirth & Tullis, 1992), who found that this transition zone, from the onset of plasticity to a regime consistent with power law creep, spanned 200 °C, independent of strain rate. The best field observations of this transition are from Stipp et al. (2002), who observed this transition on the Tonale fault in the Italian Alps. They found that the lower transition, the onset of plasticity, occurred at ~300 °C. The upper transition to a flow regime consistent with power law creep occurred at ~500 °C. The Tonale fault is a 250-km-long strike-slip transform segment between two thrusts of the Periadriadriatic fault system. Its strength-depth profile should therefore correspond to that of a thrust fault. It accommodated at least 30 km of slip during its active period in the Oligocene (Müller et al., 2001). The Tonale fault is thus probably best placed in the fast intraplate fault category (3 mm/year). The width of its shear zone is about 300 m (Stipp et al., 2002), placing it at $\dot{\varepsilon} = 3{*}10^{-13}$ 1/s. At that slip velocity and width Figure 8 indicates that the lower transition point is at 11-km depth and the upper transition at 17 km. Those depths correspond to temperatures of 300 and 450 °C, respectively, in good agreement with the field and experimental data. The temperature range over which the deformation mechanisms change will be smaller for slower strain rates. For example, the results of Dunlap et al. (1997) and Hirth et al. (2001) suggest that the BDT zone spans only about 50° at a strain rate of 10^{-16} 1/s, since it occurs at a lower T, around 300 °C. This smaller range of the BDT is just a property of the Arrhenius relationship of exp(−Q/RT), as seen in Figure 14 of Tullis (2002).

5.2. Interactions Between Seismic and Interseismic Deformation, as Predicted by the Model

The assumption that plasticity onset is controlled by real contact area saturation predicts a certain depth for the transition from frictional sliding to exponential creep, as discussed in the previous subsection. When using a typical geotherm of 25 °C/km, and a thrust stress regime, this depth is ~11 km (Figure 7), but the onset of the BDT will be deeper (shallower) in colder (hotter) locations. The BDT zone will also be pushed deeper for strike slip or normal faulting. The BDT zone predicted by our model is a zone where plastic slip coexists with frictional slip: Plasticity dominates low slip rates while frictional slip dominates fault slip at fast rates (Figure 7). The coexistence of two sliding mechanisms, predicted to occur at the same depth but for faults sliding at different rates, may explain shear zones that exhibit seemingly surprising assemblages of microstructures and behaviors.

Figure 9 depicts our suggestion for the possible lifecycle of fault zones within the low-temperature plasticity zone of the BDT: such fault zones may creep plastically for a long time as mylonites at the bottom of seismogenic fault zones (point 1 in Figure 9). A large earthquake initiating above the BDT zone can then propagate into it by virtue of increasing the slip velocity there, thereby driving it into the velocity-weakening frictional regime (2). Unstable slip then leads acceleration to coseismic slip rates that produce melting—and the resulting pseudotachylytes (3). After slip ceases and the fault cools, the fault returns to state (1) and resumes plastic flow, resulting in mylonitization of the pseudotachylytes.

Many observations of fault zones within the upper part of the BDT show pseudotachylytes penetrating into mylonites (Camacho et al., 1995; Lin et al., 2005; Passchier, 1984). Lin et al. (2005) describe pseudotachylytes in the Woodroffe thrust, Western Australia, within a 1.5-km-thick mylonitized shear zone separating

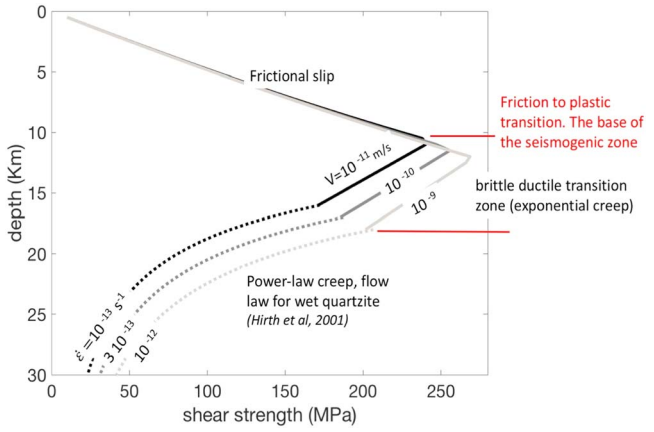

Figure 8. Quartz/granite shear strength as function of depth, for three different geological slip rates (0.3, 3, and 30 mm/year, marked on the figure in meters per second) representing three typical geologic strain rates for active thrust faults. These rates correspond to slow intraplate, fast intraplate, and interplate faults, respectively. Sliding is presumed to occur on faults with widths of 100, 300, and 1,000 m respectively, and thus represents geological strain rates of 10^{-13}, $3{\cdot}10^{-13}$, and 10^{-12} s^{-1}, respectively. The solid lines are our model calculations. The dashed lines are power law wet quartzite experimental flow laws (Hirth et al., 2001), as detailed in equation (10). Our model shows a transition from friction to exponential creep at a depth that increases with the slip rate, between 11 and 13 km. This is the friction-plastic transition that marks the upper limit of the brittle-ductile transition (BDT) zone. Exponential creep produces a linear drop in strength with depth. This regime extends down until it intersects the power law creep flow law, here at 16- to 18-km depths. The exact location of this transition between exponential creep and power law creep (the lower boundary of the BDT zone) depends on slip rate, shear zone width, the type of faulting, and other model parameters (not shown). Below this depth, power law creep dominates the deformation since it predicts lower strength for the same slip rate. Thus, we predict a BDT transition zone that ranges from 11 to 18 km, depending on conditions. This transition zone is characterized by plastically sliding faults (low-temperature plasticity), which are predicted to merge into shear zones at greater depth.

granulite facies from amphibolite facies gneisses. The shear zone, exposed at a depth of 25–30 km, contains large volumes of millimeters to centimeter scale pseudotachylyte veins. They are of two types, cataclasite related and mylonite related. The pseudotachylyte veins penetrate into mylonites and ultramylonites and are themselves overprinted by subsequent mylonitization, with foliation parallel to that of the mylonites. The cataclastic-related veins overprint the mylonite-related ones and were produced subsequent to the unroofing of the fault through the brittle-plastic transition.

We suggest that observations of seemingly cogenetic mylonite-pseudotachylite assemblages may be explained by the cycle depicted in Figure 9. In fact, observations of seemingly cogenetic mylonite-pseudotachylite assemblages are quite common in major fault zones, for example, the Outer Hebrides Fault Zone (Sibson, 1980), Redbank Shear Zone, Australia (Hobbs et al., 1986), the Silvretta Nappe, Eastern Alps (Koch & Masch, 1992), and the Møre-Trøndelag Fault Complex in central Norway (Sherlock et al., 2004). The mylonites and pseudotachylites commonly appear to be synkinematic (J. C. White, 1996) and complex formation mechanisms have been proposed to explain their paradoxical coexistence. Our model predicts these relationships in a quite straightforward manner.

Finally, our model also provides a simple physical explanation for the observation (Jiang & Lapusta, 2016) that large earthquakes may penetrate into the ductile zone, although no nucleation of earthquakes is observed within this BDT zone.

5.3. Width of the Shear Zone

In the transition zone, shearing occurs by exponential plastic creep within the fault zone material, hence producing a relatively narrow mylonitized shear zone. The power law creep law, on the other hand, refers to the bulk flow of the country rock. Therefore, the base of the BDT should correspond with a widening of the zone of shear from a narrow shear zone to a broader zone of shear deformation within the country rock. The net result is the half-hourglass shape often depicted in sketches of the region of ductile shear beneath faults. This great widening of shear zones with depth, as shown, for example, in the work of Bak et al. (1975) and Hanmer et al. (1995) was previously thought to arise from the ameliorating effect of temperature on the strength contrast between the shear zone and the surrounding rock. We now recognize that this is only part of the explanation.

6. Discussion

6.1. Model Assumptions for Plastic Behavior

A&S18 developed a model in which friction is determined by thermally activated creep of asperity contacts under steady state thermal and stress conditions. This paper extends the model to sliding under high ambient temperature and high normal stress, with an additional physical assumption added to capture the transition to plastic shear from purely frictional sliding. We propose that plasticity relates to how real contact area evolves during sliding in the following way: Thermally activated asperity creep leads to growth of real area of contact A_r. A_r growth will eventually become restricted by other process, and reach a maximum, A_r^{res}, beyond which it cannot increase further. At this point, the shear strength becomes nearly independent of normal stress, (for the stress regime that pertains to the crust, seen in Figure 5), the b term in the rate and state equation goes to 0 (equations (7a)–(7c)), and consequently, the rheology will cease to be frictional and instead will become that of low-temperature exponential plastic creep (equation (8)). We call this the FPT. The FPT can be expected to depend on minerology. For ice, frictional strength becomes independent

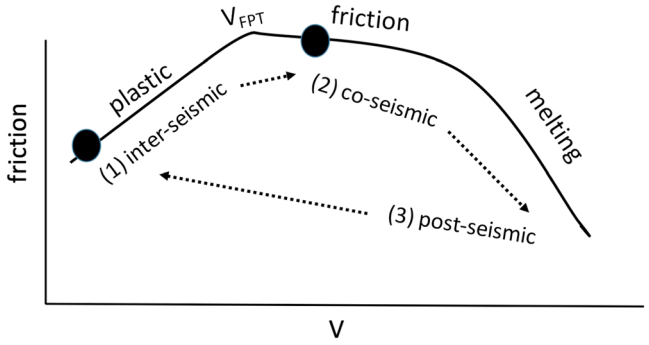

Figure 9. Cartoon illustrating lifecycles of a fault at a depth within the brittle-ductile transition (BDT) zone, inferred from model predictions. This cartoon redraws the friction-velocity dependence of Figure 7, which show that for normal geothermal conditions, at, say, 13-km sliding at high strain rate will occur by frictional slip and exhibit velocity weakening, while slow slip occurs in plastic manner. Thus, deeply buried fault zones, within the BDT of seismogenic faults, spend most of their lifetimes between earthquakes, sliding plastically as mylonites (point 1). A large earthquake that nucleates on a fault above the BDT zone may propagate downward into the BDT zone and drive motion to a slip rate that is within the frictional regime (point 2). This regime allows unstable sliding due to the velocity and thermal weakening behavior that exists for sliding at $V > V_{FPT}$. The fault will accelerate to coseismic slip rates, resulting in melting and the production of pseudotachylytes. After the earthquake is finished, the fault decelerates and cools (point 3), and sliding returns quite quickly to its interseismic mode (point 1), resuming plastic deformation. Thus, our model explains the occurrence of mylonites overprinted by pseudotachylytes within the BDT zone.

of normal stress at a sliding velocity of 5×10^{-8} m/s, a normal stress of 40 kPa, and temperature of −10 °C (Schulson & Fortt, 2012).

The value of A_r^{res} merits discussion. We have assumed that the value of A_r^{res}/A grows nonlinearly with pressure: growth is very slow and so A_r^{res}/A is nearly constant at low stress, while it approaches 1 at pressures exceeding several gigapascals. The contention that A_r^{res}/A remains much smaller than 1 under pressures of a few hundreds of megapascals is supported by fitting the data and also by an examination of the structure of the materials produced under such conditions: The deformed gouge from the high-temperature experiments of Blanpied et al. (1995) exhibits discrete sliding surfaces, of both the Riedel and Y surface (parallel to the shear direction) types. Thus, even though the rheology is that of plastic flow, deformation is not by bulk flow but largely by shear on discrete surfaces. Such surfaces must have A_r significantly less than A; otherwise, they would not be recognizable as surfaces. Natural mylonites also often exhibit discrete slip on C surfaces (so-called S/C mylonites) and the same inference may be applied to them. (n.b. that both C and Y surfaces are concordant with the shear zone. They differ only in nomenclature. The term C surface, introduced by Berthe et al., 1979, is used in the structural geology literature, the term Y surfaces, introduced by Logan et al., 1992, is used in the experimental friction literature.)

At very high pressure (>3 GPa) we predict that $\frac{A_r^{res}}{A}$ approaches 1, at which point bulk exponential flow is predicted. However, for the geological low strain rates in the crust, much before bulk low-temperature plasticity takes over, there will be a change in the deformation mechanism—the deformation will transition from exponential flow to power law creep, as predicted in Figure 8, at a depth of ~18 km which is at ~500 MPa. The transition from exponential-creep controlled sliding on discrete surfaces to power law bulk creep occurs when the contact area on the discrete surface is still quite low, $A_r^{res}/A \approx 0.1$ (see Figure 3).

6.2. Parameter Values

All parameters in our model, except for the maximum contact area, A_r^{res}/A,were carried from A&S18, where they were obtained independently using thermodynamic and material parameters and were verified against low-temperature and low normal stress experimental results. The function $A_r^{res}/A(\sigma_n)$,which is the value of real contact area achieved during plastic flow, was the single free parameter used in fitting the model to the high-temperature and normal stress experiments of Blanpied et al. (1995) and Hirth and Tullis (1994). The best fit, shown in Figure 2, uses run 4 from A&S18 and A_r^{res}/A given by equation (9). The value predicted for A_r^{res}/A at 400-MPa stress is about 0.1, which agrees within a factor of 2 with the value 0.05 found by Beeler et al. (2016, their Figure 6). For σ_n=2.25 GPa our model predicts that $\frac{A_r^{res}}{A} \approx 0.5$, that is, about 5 times larger than at 400 Mpa, but that still sliding occurs on discrete surfaces, as observed in Hirth and Tullis (1994).

The three (nonmonotonic) curves of Blanpied et al. (1995) provide multiple and tight constraints on the value of A_r^{res}/A at 400 MPa. The model predicts theoretically (see section 6.5 below) that a single value of A_r^{res}/A at 400 MPa controls the migration the FPT temperature (T_{FPT}) rightward with increasing slip rate. The $\frac{A_r^{res}}{A}$ value also controls the (linear) slope of the strength versus temperature curves in the plastic regime. It is thus reassuring that the three model-predicted values for T_{FPT} in Figure 2 (one for each slip rate) agree well with the data and that our model captures correctly the slope linearity and its three different values (one for each slip rate). A&S18 (their Figure 8) showed also the good fit of the same model and parameters to low temperature and stress experiments in Tonalite, Novaculite, quartz and granite, as compiled by Di Toro et al. (2011). These multiple fits lend confidence to the model and also to the value of $\frac{A_r^{res}}{A}$ at this stress and to the hypothesis that $\frac{A_r^{res}}{A}$ is independent of T_0.

At this point, there is no theory to calculate $\frac{A_r^{res}}{A}$,and such a theory will be an important advancement in the future. In addition, there is also need for more measurements of friction at elevated normal stress, since currently there are only the single set of Blanpied et al. (1995) measurements at 400 MPa and the one data point of steady state friction at 2.2 GPa from Hirth and Tullis (1994).

6.3. The FPT Relation to the *a* and *b* Parameters

As explained in A&S18, the a and b terms have a definite physical interpretation revealed by our model: a measures the effect of slip rate on contact shear strength, while b measures the effect of time or slip rate on contact area growth. A&S18 calls a the viscous shear term and b the contact area growth term, based on their physical origin. A&S18 investigated steady sliding in the frictional regime (under low T and σ_n), deriving from equations (3a)–(3e) and (4) a frictional law (equations (6a)–(6d) here) that predicts a generalized form of the empirical rate and state laws.

In this paper, we use this same derivation to investigate sliding at the plastic regime (under high T_0 and σ_n). Our assumption that contact area saturates in plasticity implies that b disappears, as seen in the plastic strength equations (7a)–(7c). Thus, in plasticity all effects of area growth, that is, of the cutoff time t_c and b, drop out, leaving only the shear creep effect, described by the viscous term a. From equations (7a)–(7c) one can easily see that in the plastic flow regime $\frac{\partial \mu_{ss}}{\partial \ln(V)} = a$. Since $a > 0$ then, as long as temperature is constant, the viscous term remains velocity strengthening, so plastic slip is velocity strengthening at low and intermediate slip rate. Only at very high slip rates thermal softening is predicted (see equation 10 of A&S18).

6.4. The FPT as Function of Slip Rate

The transition from frictional to plastic behavior is set in our model by choosing $\frac{A_r^{res}}{A}$. We found $\frac{A_r^{res}}{A}$ by fitting our model to the experimental results in Figure 2. Using this $\frac{A_r^{res}}{A}$ predicts that slip at geological strain rates, becomes plastic at about 330 MPa and 300 °C, corresponding to ~11 km depth. Shear is plastic only for $V < V_{FPT}$, while faster slip still is frictional (Figures 6 and 7). The reason that plasticity occurs only during slow slip is because slow slip allows contacts sufficient time to grow during their lifetime and reach the saturated contact area, which is the criteria for plasticity onset. The same effect (seen in Figure 7) of plasticity prevailing at faster slip rates with increasing ambient temperature was also seen experimentally by Chester and Higgs (1992), as shown in Figure 1b, by noting that the point at which the friction slope changes migrates to the right with increasing T.

6.5. Friction and Strength as Function of Temperature

Run 4 fits both the rise of friction with ambient temperature before the FPT and the drop of strength with ambient temperature after the FPT, following closely the data of Blanpied et al. (1995), as seen in Figure 2. Not all of the runs that fit the low T, low σ_n data in A&S18 fit the high-T and high σ_n data so well. In the crudest sense, the data in Figure 2 poses two constraints: In the frictional regime, friction must increase with T_0, while in the plastic regime strength should decrease approximately linearly with T_0. From equations (6a)–(6d) and (7a)–(7c) one can calculate $\frac{\partial \mu}{\partial T}$ in the two regimes while posing these constrains:

$$\frac{\partial \mu^f}{\partial T_c} \sim \frac{\partial a^*}{\partial T_c} \ln\left(\frac{V}{V_{smax}}\right) + \frac{\partial b^*}{\partial T_c} \ln\left(1 + \frac{d}{t_c V}\right) + \frac{\partial \ln\left(1 + \frac{d}{t_c V}\right)}{\partial T_c} b^* > 0 \tag{11a}$$

and

$$\frac{\partial \mu^p}{\partial T_c} = \frac{\partial a}{\partial T_c} \ln\left(\frac{V}{V_{smax}}\right) < 0 \tag{11b}$$

We shall first analyze the plastic regime, equation (11b): using equations (7a)–(7c) we see that $\frac{\partial a}{\partial T_c} = \frac{A_r^{res}}{A\sigma_n} \frac{Q_\delta}{N\Omega_s}$ (all positive parameters). Since $V_{smax} \gg V$,then all minerals fulfill the condition in equation (11b) that $\frac{\partial \mu^p}{\partial T_c} < 0$, exhibiting thermal softening in plastic flow. In fact, equation (11b) predicts a material-independent *linear* drop of strength with ambient temperature in the plastic regime, with a slope that depends on the slip

rate, as seen in Figure 2. The linear drop of μ^p with T_c depends on the assumption that $A_r^{res} = const$. If A_r^{res} grows with T, then $\frac{\partial a}{\partial T_c}$ will not be constant and there will not be a linear trend.

The value of the linear slope depends on several tightly constrained parameters (N, R) and on several less constrained parameters ($\frac{A_r^{res}}{A}, \Omega_s, V_{smax}$). The values of activation volume, Ω_s, and V_{smax} were discussed in A&S18 and constrained in the different runs presented there for the low T_0 and σ_n experiments. The value of A_r^{res}/A at this stress (found to be equal to 0.096) was the sole free parameter to constrain the linear slopes of strength versus T_0 within the curves in Figure 2.

Next we look at the frictional regime: The data-dictated condition in equation (11a), that is, that $\frac{\partial \mu^f}{\partial T_c} > 0$ in the frictional regime, is less trivial and is only met under certain values of the a^* and b^* prefactors. In fact, when plugging in parameters values from Table 1, it is concluded that without considering the temperature dependence of σ_c^0,this condition is not met and $\frac{\partial \mu^f}{\partial T_c} < 0$. Friction is thermally strengthening in the frictional regime only if one also considers the temperature dependence of σ_c^0 and assumes the ab initio contact stress decreases (i.e., ab initio contact area increases) with increasing T_0. This dependence is in turn dictated in our model by the B parameter dependence on T_0, as discussed in A&S18. We used here, and in A&S18, experimental σ_c^0 dependence on T_0 taken from quartz indentation experiments of Evans (1984), his Figure 5, which was enough to ensure the thermal strengthening observed here in the frictional regime.

One may ask why here in Figure 2 the high-T experiments show thermal strengthening in the frictional regime, while in A&S18, the low T and low normal stress experiments show thermal softening at high velocities. Equation 10 of A&S18 shows that under moderate and high V the b term is negligible, and if σ_c^0 is taken as constant with temperature, thermal softening will prevail. Strengthening is obtained only if one assumes the ab initio contact area increases with increasing T_0. In fitting the low T_0 experiments in A&S18, σ_c^0 was taken constant since we assumed contacts heated up only during sliding one against another and are initially cold at the first nanosecond of any two contacts meeting. In contrast, here under elevated T_0, the temperature dependence of σ_c^0 was taken into account, and we used σ_c^0 that decreases with T_0, following Figure 5 of Evans (1984). Also, the sliding velocities here are low and the b term (the contact growth term) is not negligible. The increase in friction due to σ_c^0 dependence on T_0 and due to contact growth during sliding, offsets the thermal softening effect of the viscous (i.e., the a) term.

6.6. The Linear Strength Drop Within the BDT Zone

The dependence of strength on temperature is also what gives rise to the linear drop in strength with depth in the low-T plasticity regime that defines the BDT in Figure 8. This can be seen by investigating how strength changes with depth in the crust:

$$\frac{\partial \tau^p}{\partial z} = \frac{\partial \tau^p}{\partial \sigma_n}\frac{\partial \sigma_n}{\partial z} + \frac{\partial \tau^p}{\partial T}\frac{\partial T}{\partial z} \tag{12a}$$

From equation (7c) we see that the only dependence of τ^p on σ_n in the plastic regime is via the dependence of $\frac{A_r^{res}}{A}$ on σ_n. Since $\frac{A_r^{res}}{A}$ is nearly constant in the low stress regime of the upper crust (<700 MPa), the first term drops, and using equation (11b), we can then approximate equation (12a) as follows:

$$\frac{\partial \tau^p}{\partial z} \approx k\frac{\partial \tau^p}{\partial T} \approx k\frac{A_r^{res} Q_s}{AN\Omega_s}\ln\left(\frac{V}{V_{smax}}\right). \tag{12b}$$

Where $k = \frac{\partial T}{\partial z}$ is the geothermal gradient. Equation (12b) predicts that the strength in the BDT zone will drop nearly linearly with depth, with a slope that depends on the slip rate, as seen in Figure 8.

6.7. Comparison to Other Work

Previous work has attempted to fit high-T and high normal stress experiments mostly via empirical laws and functional fitting: Blanpied et al. (1995) fit their data using the rate and state friction law to which was added an empirical temperature dependence due to Chester (1994, 1995). This was originally developed to fit the data of Chester and Higgs (1992). Shimamoto and Noda (2014) represent the FPT by a ratio of

macroscopic empirical laws for friction and flow with a smooth transition by a tan*h* function. These models are not qualitatively different from the two-state model such as Brace and Kohlstedt (1980). They can fit the data but do not contain a theory that predicts the data.

Acknowledgments
This work was funded by ISF grant 910/17. We thank G. Hirth and an anonymous reviewer for their thorough reviews that improved the manuscript greatly. This paper is theoretical and does not contain any new data.

References

Aharonov, E., & Scholz, C. H. (2018). A physics-based rock friction constitutive law: Steady state friction. *Journal of Geophysical Research: Solid Earth*, *123*, 1591–1614. https://doi.org/10.1002/2016JB013829

Bak, J., Korstgard, J., & Sorensen, K. (1975). Major shear zone within Nagssugtoqidian of West Greenland. *Tectonophysics*, *27*(3), 191–209. https://doi.org/10.1016/0040-1951(75)90016-5

Baumberger, T., & Caroli, C. (2006). Solid friction from stick–slip down to pinning and aging. *Advances in Physics*, *55*(3–4), 279–348. https://doi.org/10.1080/00018730600732186

Beeler, N. M., Hirth, G., Thomas, A., & Bürgmann, R. (2016). Effective stress, friction, and deep crustal faulting. *Journal of Geophysical Research: Solid Earth*, *121*, 1040–1059. https://doi.org/10.1002/2015JB012115

Beeler, N. M., Tullis, T. E., & Goldsby, D. L. (2008). Constitutive relationships and physical basis of fault strength due to flash heating. *Journal of Geophysical Research*, *113*, B01401. https://doi.org/10.1029/2007JB004988

Behr, W. M., & Platt, J. P. (2011). A naturally constrained stress profile through the middle crust in an extensional terrane. *Earth and Planetary Science Letters*, *303*(3–4), 181–192.

Berthe, D., Choukroune, P., & Jegouzo, P. (1979). Orthogneiss, mylonite and non-coaxial deformation of granites: The example of the South Armorican shear zone. *Journal of Structural Geology*, *1*(1), 31–42. https://doi.org/10.1016/0191-8141(79)90019-1

Blanpied, M. L., Lockner, D. A., & Byerlee, J. D. (1995). Frictional slip of granite at hydrothermal conditions. *Journal of Geophysical Research*, *100*(B7), 13,045–13,064.

Bowden, F. P., & Tabor, D. (1950). *The friction and lubrication of solids* (Vol. 1). Oxford: Clarendon Press.

Bowden, F. P., & Tabor, D. (1964). *The friction and lubrication of solids* (Vol. 2). Oxford: Clarendon Press.

Brace, W. F., & Kohlstedt, D. L. (1980). Limits on lithospheric stress imposed by laboratory experiments. *Journal of Geophysical Research*, *85*(B11), 6248–6252. https://doi.org/10.1029/JB085iB11p06248

Brechet, Y., & Estrin, Y. (1994). The effect of strain rate sensitivity on dynamic friction of metals. *Scripta Metallugica et Materialia*, *30*(11), 1449–1454. https://doi.org/10.1016/0956-716X(94)90244-5

Camacho, A., Vernon, R. H., & Fitz Gerald, J. D. (1995). Large volumes of anhydrous Pseudotachylyte in the Woodroffe Thrust, Eastern Musgrave Ranges, Australia. *Journal of Structural Geology*, *17*(3), 371–383. https://doi.org/10.1016/0191-8141(94)00069-C

Chen, J., & Spiers, C. J. (2016). Rate and state frictional and healing behavior of carbonate fault gouge explained using microphysical model. *Journal of Geophysical Research: Solid Earth*, *121*, 8642–8665. https://doi.org/10.1002/2016JB013470

Chester, F. M. (1994). Effects of temperature on friction: Constitutive equations and experiments with quartz gouge. *Journal of Geophysical Research*, *99*(B4), 7247–7261. https://doi.org/10.1029/93JB03110

Chester, F. M. (1995). A rheologic model for wet crust applied to strike-slip faults. *Journal of Geophysical Research*, *100*(B7), 13,033–13,033, 13044. https://doi.org/10.1029/95JB00313

Chester, F. M., & Higgs, N. G. (1992). Multimechanism friction constitutive model for ultrafine quartz gouge at hypocentral conditions. *Journal of Geophysical Research*, *97*(B2), 1859–1870. https://doi.org/10.1029/91JB02349

Di Toro, G., Goldsby, D. L., & Tullis, T. E. (2004). Friction falls towards zero in quartz rock as slip velocity approaches seismic rates. *Nature*, *427*(6973), 436–439. https://doi.org/10.1038/nature02249

Di Toro, G., Han, R., Hirose, T., De Paola, N., Nielsen, S., Mizoguchi, K., et al. (2011). Fault lubrication during earthquakes. *Nature*, *471*(7339), 494–498. https://doi.org/10.1038/nature09838

Dieterich, J. H. (1972). Time-dependent friction in rocks. *Journal of Geophysical Research*, *77*(20), 3690–3697. https://doi.org/10.1029/JB077i020p03690

Dieterich, J. H. (1978). Time-dependent friction and the mechanics of stick-slip. *Pure and Applied Geophysics*, *116*(4–5), 790–806. https://doi.org/10.1007/BF00876539

Dunlap, W. J., Hirth, G., & Teyssier, C. (1997). Thermomechanical evolution of a ductile duplex. *Tectonics*, *16*(6), 983–1000. https://doi.org/10.1029/97TC00614

Evans, B. (1984). The effect of temperature and impurity content on indentation hardness of quartz. *Journal of Geophysical Research*, *89*(B6), 4213–4222.

Evans, B., & Goetze, C. (1979). The temperature variation of hardness of olivine and its implication for polycrystalline yield stress. *Journal of Geophysical Research*, *84*(B10), 5505–5524. https://doi.org/10.1029/JB084iB10p05505

Goetze, C., & Evans, B. (1979). Stress and temperature in the bending lithosphere as constrained by experimental rock mechanics. *Geophysical Journal International*, *59*(3), 463–478. https://doi.org/10.1111/j.1365-246X.1979.tb02567.x

Hanley, E. J., Dewitt, D. P., & Roy, R. F. (1978). The thermal diffusivity of eight well-characterized rocks for the temperature range 300–1000 K. *Engineering Geology*, *12*, 31–47. https://doi.org/10.1016/0013-7952(78)90003-0

Hanmer, S., Williams, M., & Kopf, C. (1995). Modest movements, spectacular fabrics in an intracontinental deep-crustal strike-slip-fault—Striding-Athabasca Mylonite Zone, Nw Canadian Shield. *Journal of Structural Geology*, *17*(4), 493–507. https://doi.org/10.1016/0191-8141(94)00070-G

Heslot, F., Baumberger, T., Perrin, B., Caroli, B., & Caroli, C. (1994). Creep, stick-slip, and dry friction dynamics: Experiments and a heuristic model. *Physical Review E*, *49*(6), 4973–4988. https://doi.org/10.1103/PhysRevE.49.4973

Hirth, G., & Beeler, N. M. (2015). The role of fluid pressure on frictional behavior at the base of the seismogenic zone. *Geology*, *43*(3), 223–226. https://doi.org/10.1130/G36361.1

Hirth, G., Teyssier, C., & Dunlap, J. W. (2001). An evaluation of quartzite flow laws based on comparisons between experimentally and naturally deformed rocks. *International Journal of Earth Sciences*, *90*(1), 77–87. https://doi.org/10.1007/s005310000152

Hirth, G., & Tullis, J. (1992). Dislocation creep regimes in quartz aggregates. *Journal of Structural Geology*, *14*(2), 145–159. https://doi.org/10.1016/0191-8141(92)90053-Y

Hirth, G., & Tullis, J. (1994). The brittle-plastic transition in experimentally deformed quartz aggregates. *Journal of Geophysical Research*, *99*(B6), 11,731–11,747. https://doi.org/10.1029/93JB02873

Hobbs, B. E., Ord, A., & Teyssier, C. (1986). Earthquakes in the ductile regime? *Pure and Applied Geophysics*, *124*(1–2), 309–336. https://doi.org/10.1007/BF00875730

Hull, J. (1988). Thickness-displacement relationships for deformation zones. *Journal of Structural Geology*, *10*(4), 431–435. https://doi.org/10.1016/0191-8141(88)90020-X

Jiang, J., & Lapusta, N. (2016). Deeper penetration of large earthquakes on seismically quiescent faults. *Science*, *352*(6291), 1293–1297. https://doi.org/10.1126/science.aaf1496

Koch, N., & Masch, L. (1992). Formation of Alpine mylonites and pseudotachylytes at the base of the Silvretta nappe, Eastern Alps. *Tectonophysics*, *204*(3-4), 289–306. https://doi.org/10.1016/0040-1951(92)90313-U

Lin, A. M., Maruyama, T., Aaron, S., Michibayashi, K., Camacho, A., & Kano, K. I. (2005). Propagation of seismic slip from brittle to ductile crust: Evidence from pseudotachylyte of the Woodroffe thrust, central Australia. *Tectonophysics*, *402*(1–4), 21–35. https://doi.org/10.1016/j.tecto.2004.10.016

Logan, J. M., Dengo, C. A., Higgs, N. G., & Wang, Z. Z. (1992). Fabrics of experimental fault zones: Their development and relationship to mechanical behavior. In B. Evans & T.-F. Wong (Eds.), *Fault mechanics and transport properties of rock* (pp. 33–68). New York: Academic.

Marone, C., Raleigh, C. B., & Scholz, C. H. (1990). Frictional behavior and constitutive modeling of simulated fault gouge. *Journal of Geophysical Research*, *95*(B5), 7007–7025. https://doi.org/10.1029/JB095iB05p07007

Mei, S., Suzuki, A. M., Kohlstedt, D. L., Dixon, N. A., & Durham, W. B. (2010). Experimental constraints on the strength of the lithospheric mantle. *Journal of Geophysical Research*, *115*, B08204. https://doi.org/10.1029/2009JB006873

Müller, W., Prosser, G., Mancktelow, N. S., Villa, I. M., Kelley, S. P., Viola, G., & Oberli, F. (2001). Geochronological constraints on the evolution of the Periadriatic Fault System (Alps). *International Journal of Earth Sciences*, *90*(3), 623–653. https://doi.org/10.1007/s005310000187

Nakatani, M. (2001). Conceptual and physical clarification of rate and state friction: Frictional sliding as a thermally activated rheology. *Journal of Geophysical Research*, *106*(B7), 13,347–13,380.

Nakatani, M., & Scholz, C. H. (2004a). Frictional healing of quartz gouge under hydrothermal conditions: 1. Experimental evidence for solution transfer healing mechanism. *Journal of Geophysical Research*, *109*, B07201. https://doi.org/10.1029/2001JB001522

Nakatani, M., & Scholz, C. H. (2004b). Frictional healing of quartz gouge under hydrothermal conditions: 2. Quantitative interpretation with a physical model. *Journal of Geophysical Research*, *109*, B07202. https://doi.org/10.1029/2003JB002938

Niemeijer, A. R., & Spiers, C. J. (2007). A microphysical model for strong velocity weakening in phyllosilicate-bearing fault gouges. *Journal of Geophysical Research*, *112*, B10405. https://doi.org/10.1029/2007JB005008

Noda, H. (2008). Frictional constitutive law at intermediate slip rates accounting for flash heating and thermally activated slip process. *Journal of Geophysical Research*, *113*, B09302. https://doi.org/10.1029/2007JB005406

Passchier, C. (1984). The generation of ductile and brittle deformation bands in a low-angle mylonite zone. *Journal of Structural Geology*, *6*(3), 273–281. https://doi.org/10.1016/0191-8141(84)90051-8

Putelat, T., Dawes, J. H., & Willis, J. R. (2011). On the microphysical foundations of rate-and-state friction. *Journal of the Mechanics and Physics of Solids*, *59*(5), 1062–1075. https://doi.org/10.1016/j.jmps.2011.02.002

Rice, J. R. (2006). Heating and weakening of faults during earthquake slip. *Journal of Geophysical Research*, *111*, B05311. https://doi.org/10.1029/2005JB004006

Rice, J. R., Lapusta, N., & Ranjith, K. (2001). Rate and state dependent friction and the stability of sliding between elastically deformable solids. *Journal of the Mechanics and Physics of Solids*, *49*(9), 1865–1898. https://doi.org/10.1016/S0022-5096(01)00042-4

Schulson, E. M., & Fortt, A. L. (2012). Friction of ice on ice. *Journal of Geophysical Research*, *117*, B12204. https://doi.org/10.1029/2012JB009219

Sherlock, S. C., Watts, L. M., Holdsworth, R. E., & Roberts, D. (2004). Dating fault reactivation by Ar/Ar laserprobe: An alternative view of apparently cogenetic mylonite–pseudotachylite assemblages. *Journal of the Geological Society*, *161*(3), 335–338. https://doi.org/10.1144/0016-764903-160

Shimamoto, T., & Noda, H. (2014). A friction to flow constitutive law and its application to a 2-D modeling of earthquakes. *Journal of Geophysical Research: Solid Earth*, *119*, 8089–8106. https://doi.org/10.1002/2014JB011170

Sibson, R. H. (1980). Transient discontinuities in ductile shear zones. *Journal of Structural Geology*, *2*(1–2), 165–171. https://doi.org/10.1016/0191-8141(80)90047-4

Sibson, R. H. (1982). Fault zone models, heat flow, and the depth distribution of earthquakes in the continental crust of the United States. *Bulletin of the Seismological Society of America*, *72*(1), 151–163.

Siman-Tov, S., Aharonov, E., Boneh, Y., & Reches, Z. E. (2015). Fault mirrors along carbonate faults: Formation and destruction during shear experiments. *Earth and Planetary Science Letters*, *430*, 367–376.

Simpson, C. (1985). Deformation of granitic rocks across the brittle-ductile transition. *Journal of Structural Geology*, *7*(5), 503–511. https://doi.org/10.1016/0191-8141(85)90023-9

Stipp, M., StuÈnitz, H., Heilbronner, R., & Schmid, S. M. (2002). The eastern Tonale fault zone: A 'natural laboratory' for crystal plastic deformation of quartz over a temperature range from 250 to 700 C. *Journal of Structural Geology*, *24*(12), 1861–1884. https://doi.org/10.1016/S0191-8141(02)00035-4

Tsenn, M. C., & Carter, N. L. (1987). Upper limits of power law creep of rocks. *Tectonophysics*, *136*(1-2), 1–26. https://doi.org/10.1016/0040-1951(87)90332-5

Tullis, J. (2002). Deformation of granitic rocks: experimental studies and natural examples. *Reviews in Mineralogy and Geochemistry*, *51*(1), 51–95.

Turcotte, D., & Schubert, G. (2014). *Geodynamics*. Cambridge: Cambridge University Press. https://doi.org/10.1017/CBO9780511843877

Voll, G. (1976). Recrystallization of quartz, biotite, and feldspars from Erstfeld to the Levantina nappe, Swiss Alps, and its geological implications. *Schweizerische Mineralogische und Petrographische Mitteilungen*, *56*, 641–647.

Vosteen, H. D., & Schellschmidt, R. (2003). Influence of temperature on thermal conductivity, thermal capacity and thermal diffusivity for different types of rock. *Physics and Chemistry of the Earth, Parts A/B/C*, *28*(9-11), 499–509. https://doi.org/10.1016/S1474-7065(03)00069-X

White, J. C. (1996). Transient discontinuities revisited: Pseudotachylyte, plastic instability and the influence of low pore fluid pressure on deformation processes in the mid-crust. *Journal of Structural Geology*, *18*(12), 1471–1486. https://doi.org/10.1016/S0191-8141(96)00059-4

White, S., Burrows, S., Carreras, J., Shaw, N., & Humphreys, F. (1980). On mylonites in ductile shear zones. *Journal of Structural Geology*, *2*(1-2), 175–187. https://doi.org/10.1016/0191-8141(80)90048-6